INORGANIC CHEMISTRY FRONTIERS

RESEARCH ARTICLE

View Article Online
View Journal | View Issue

Cite this: *Inorg. Chem. Front.*, 2026, **13**, 2008

A low-loss optical waveguide from a 1D europium nanocluster

Jingjing Xia,†[a] Weinan Dong,†[a] Shengrong He,[a] Feng Jiang,*[a] Wenming Tian, *[b] Qi Sun, [b] Meixin Hong,[a] Lingchen Meng,[a] Yu Zhang, [a] Zhennan Wu, *[a] Tingting Li*[c] and Xue Bai *[a]

Received 20th November 2025,
Accepted 24th December 2025

DOI: 10.1039/d5qi02356d

rsc.li/frontiers-inorganic

The rational engineering of material properties and spatial arrangements enabling micro–nano-optical waveguides is crucial for realizing photonic integration and particularly for processing ultracompact optical signal platforms. Rare-earth ions have narrow-band emission and long excited-state lifetimes stemming from stable 4f energy-level structures, which enable extremely low non-uniform linewidths and very small spectral spreads to achieve high-resolution and high-fidelity optical signal transmission in waveguides. Herein, we reported a low-loss optical waveguide with a coefficient of 6.4×10^{-3} dB μm^{-1} from the electric dipole $^5D_0 \rightarrow {}^7F_2$ transition in one-dimensional europium nanoclusters, the minimum value for rare earth-based materials. The structural orientations and luminescence performance associated with optical waveguides have also been explored in depth. The effectively directed photon transport makes lanthanide-based metal nanoclusters promising candidates for active photonic elements.

Introduction

Optical waveguides realize optical amplification, optical modulation, and other functions through constraining and transmitting optical signals.[1–7] Depending on their structure, shape and arrangement, different materials have specific advantages in terms of light transmission.[8–11] Inorganic semiconductors with extremely high refractive indices provide a strong confinement capacity for light but suffer from prohibitively high manufacturing costs.[12,13] Organic emitters, despite their superior design flexibility and processability, incur substantial optical losses and exhibit poor stability.[14,15] Polymer waveguides are simple to produce, yet they demonstrate pronounced anisotropic light scattering losses due to their amorphous microstructure resulting from random molecular orientation and chain entanglement defects.[16,17] The Information Age has placed higher demands on the performance of micro–nano-optical waveguides, and superior fabrication materials are urgently required.

Rare-earth nanocluster-based optical waveguides are emerging as promising devices that feature low cost and easy processing. More importantly, given the shielding effect on 4f electrons, rare-earth ions exhibit exceptional optical stability, high color purity and long lifetimes. Nanocluster materials as editable minimal units can confine rare-earth ions within molecular dimensions *via* organic ligand binding, forming periodic, stable coordination networks and allowing efficient directional photon transmission. However, progress in rare-earth nanocluster optical waveguides is lagging behind. On the one hand, the complex solution environment prevents the nanocluster units from developing long-range ordered assemblies, causing massive light scattering due to defects. On the other hand, the luminescence of rare-earth ions is influenced by multiple factors, including ligand vibrations, lattice symmetry, and the crystal field environment, which tend to result in low emission efficiency. Therefore, low-loss optical waveguides from rare-earth nanoclusters are still far from ideal and deserve extensive attention.

Herein, we reported a one-dimensional (1D) europium nanocluster (Eu-NC) microcrystal that shows an optical waveguide with a low-loss coefficient of 6.4×10^{-3} dB μm^{-1}, originating from the Eu^{3+} electric dipole transition. Protective ligands such as methoxybenzoic acid (MOBA) induce Eu-NCs to assemble into a highly ordered arrangement of 1D crystal structures through abundant inter-cluster π–π and C–H···π interactions. The ligand's vibration is the major non-radiating source. J–O theory analysis indicates that the luminescence of Eu-NCs is also strongly affected by the lattice symmetry and

[a]*State Key Laboratory of Integrated Optoelectronics, JLU Region, College of Electronic Science and Engineering, Jilin University, 2699 Qianjin Street, Changchun, 130012, P. R. China. E-mail: jiangfeng25@jlu.edu.cn, wuzn@jlu.edu.cn, baix@jlu.edu.cn*
[b]*State Key Laboratory of Molecular Reaction Dynamics, Dalian Institute of Chemical Physics, Chinese Academy of Sciences, 457 Zhong Shan Road, Dalian 116023, P. R. China. E-mail: tianwm@dicp.ac.cn*
[c]*College of Materials Science and Engineering, Jilin Jianzhu University, Changchun 130012, P. R. China. E-mail: litingting@jlju.edu.cn*
†These authors contributed equally to this work.

crystal field environment. The systematic structural and optoelectronic features of rare-earth NCs suggest promising applications as active photon-transport materials in next-generation miniaturized optical communication systems and photonic integrated circuits.

Experimental

Materials and reagents

4-Methoxybenzoic acid (MOBA, 98%) was purchased from Aladdin Reagent Co. (Shanghai, China). $Eu(NO)_3{\cdot}6H_2O$ (99.9%) was purchased from Macklin Biochemical Technology Co. (Shanghai, China). Anhydrous ethyl alcohol (EtOH, ≥99.7%) was purchased from China Pharmaceutical Group. Millipore water (18.2 MΩ) was used throughout the experiments. All chemicals were used as received without additional purification.

Preparation of the Eu-NC

We synthesized the crystals described herein using the hydrothermal synthesis strategy developed previously. 4-Methoxybenzoic acid (0.03 g, 0.20 mmol) and $Eu(NO)_3{\cdot}6H_2O$ (0.27 g, 0.6 mmol) were added to 3 mL of EtOH and 4 ml of H_2O and were fully dissolved. The pH value of the reaction solution was adjusted to 4.0–5.0 using aqueous NaOH solution (1.0 M) under stirring and then heated to 70 °C for 12 h.

X-ray crystallography

Single-crystal X-ray diffraction data for the Eu-NC were recorded on a Bruker Apex CCD ll area-detector diffractometer with graphite-monochromated MoKα radiation (λ = 0.71073 Å) at 100 K. Absorption corrections were applied using a multi-scan technique and performed by using the SADABS program. The structure of the Eu-NC was solved using direct methods and refined on F^2 by full-matrix least squares methods by using the SHELXTL minimization on the Olex2 software package (CCDC number: 1459317 for the Eu-NC). During the refinement, all the non-H atoms were refined anisotropically.

Polarization and waveguide measurements

A home-built photoluminescence (PL) scanning imaging microscope was used to map the PL and polarization within the crystal. Excitation of the sample was achieved with a UV laser (375 nm, Fianium, UK). For partial excitation measurement, the same excitation laser beam was fixed at a specific crystal position with a spot radius of ~0.6 μm through the same objective lens. PL image measurements were collected by fast rotation of a galvanometer mirror and using a high-speed detector (HPM-100-50, Hamamatsu, Japan) with a 450 nm long pass filter. Each scanning image contains 256 × 256 pixels. A 0.5 mm pinhole was placed before the detector to ensure that only PL from a diffraction-limited spot was observed. The magnification, M, from the sample plane into the pinhole is M = $20.8{\cdot}M_{\mathrm{lens}}$ = 2080 (where M_{lens} is the magnification of the objective lens, and 20.8 is the magnification in the scan head). The theoretical PL collection spot diameter (d_{PL}) was calculated by dividing the pinhole size with the magnification $d_{\mathrm{PL}} = d_{\mathrm{pinhole}}/M$ = 240 nm, which was smaller than the radius of the Airy disc ($r_{\mathrm{Airy\ disc}} = 0.61\lambda/\mathrm{N.A.} = 0.61 \times 708/0.95 = 455$ nm with the emission spectrum centered at 610 nm). To obtain steady-state fluorescence emission spectra, a setup that mainly consisted of a monochromator (SpectraPro-2300i, Acton Research Co., USA) and an intensified charge-coupled device (ICCD) camera (PI-MAX: 1024HB, USA) was used, sharing the same excitation source and microscope objective for signal collection. The slit in the monochromator is 0.02 mm, which ensures that the PL collection area is small enough.

Characterization

Photoluminescence (PL) and photoluminescence excitation (PLE) and luminescence decay curves over a wide scanning range were recorded with an FLS1000 spectrofluorometer. X-ray photoelectron spectroscopy (XPS) was conducted on a Thermo Scientific ESCALAB250 spectrometer equipped with a monochromatic Al Kα radiation source (1486.6 eV). Fourier transform infrared (FTIR) spectroscopy was performed using a Nicolet iS50 spectrometer (Thermo Fisher). Powder X-ray diffraction (XRD) was performed on a Rigaku SmartLab SE diffractometer. Thermogravimetric analysis (TGA, ~3 mg of sample used) was conducted under nitrogen atmosphere (flow rate ~50 mL min^{-1}) at a heating rate of 10 °C min^{-1} using a TGA550 analyzer (Waters). Scanning electron microscopy (SEM) was performed using a Hitachi Regulus 8100. Solid-state UV-vis spectra were collected using a Lambda 1050+. The absolute PL quantum yields (QYs) of the samples were measured using the FLS1000 spectrometer with the entry and output ports of the sphere located at 90° relative to each other in the plane of the spectrometer. A standard tungsten lamp was used to correct the optical response of the instrument. For low-temperature measurements, samples were mounted on a closed cycle cryostat (20–300 K, DE202, Advanced Research Systems). All the spectral data were recorded at RT by using the powder samples unless otherwise noted and corrected for the spectral response of both the spectrometer and the integrating sphere.

Experimental and theoretical intensity parameters

The theoretical background of 4f–4f intensity theory is well established and widely used in the lanthanides especially in trivalent europium compounds. The intensities of 4f–4f transitions in Eu^{3+} complexes are usually expressed in terms of the areas under the curves in their emission spectra. From these spectra, the experimental intensity parameter Ω_2 may be estimated using the equation

$$\frac{A_{\mathrm{ed}}}{A_{\mathrm{md}}} = \frac{\int I_{\mathrm{J}}(\nu)\mathrm{d}\nu}{\int I_{\mathrm{md}}(\nu)\mathrm{d}\nu} = \frac{e^2}{S_{\mathrm{md}}}\frac{{\nu_{\mathrm{J}}}^3}{{\nu_{\mathrm{md}}}^3}\frac{(n^2+2)^2}{9n^2}$$

$$\Omega_{J'}|\langle \psi J||U^{(J')}||\psi' J'\rangle|^2 \quad (J = 2, 4)$$

where A_{ed} and A_{md} on the left of the equation are the electric dipole transition and magnetic dipole transition rates, respectively, and their ratio can be acquired by calculating the inte-

grated area ratio of the corresponding emission spectra. On the right of the equation, the magnetic line strength S_{md} = 1.07×10^{-41} cm^{-1}, $e = 1.6 \times 10^{-19}$ C, ν_J stands for the transition energy barycenter and n is the refractive index; the $|\langle \psi J || U^{(J')} || \psi' J' \rangle|^2$ values are 0.0032 and 0.002.

Results and discussion

The Eu-NC was prepared based on previously developed colloidal methods by mixing MOBA and $Eu(NO_3)_3 \cdot 6H_2O$ in EtOH and H_2O at a particular ratio.[18,19] After adjusting the pH, a final clarified solution was obtained. The solution was then subjected to 70 °C to allow the target product to reach a supersaturated state for crystallization and precipitation. The crystallized Eu-NC presents a transparent rod-like morphology (Fig. S1). Single-crystal X-ray diffraction (SCXRD) analysis reveals that the Eu-NC crystallizes in the monoclinic system with the space group $P21/c$ and exhibits unit cell parameters of a = 7.69 Å, b = 22.22 Å, and c = 13.41 Å. The detailed crystal data are summarized in Table S1. The overall structure is $[Eu(MOBA_3)]_2$, where the smallest asymmetric unit is composed of one Eu ion and three deprotonated ligands (Fig. 1a). The Eu ion is coordinated by eight carboxylate oxygen atoms, which present a distorted double-capped trigonal prismatic geometry. In this vein, X-ray photoelectron spectroscopy (XPS) further verified the valence states of europium (Eu^{3+}) and oxygen (O^{2-}) (Fig. S2). The two asymmetric units are connected by the carboxyl group on the ligand and are linked *via* carboxylate groups in an offset rotation of 180°, propagating into a 1D coordination chain structure. These chains are further packed into a three-dimensional framework primarily stabilized by interactions between adjacent aromatic rings that involve both π–π stacking and C–H···π bonds (Fig. 1b–d). To gain further insight into intermolecular interactions, Hirshfeld Surface (HS) analysis was performed, which highlights intermolecular contact regions. The HS maps reveal that π–π contacts dominate the intercluster surface interactions, accounting for 40.8% of the total, indicative of strong non-covalent attraction that contributes to enhanced structural rigidity (Fig. 1e and f). In addition, potential atomic contacts are also listed in Fig. 1g, with red and blue areas corresponding to high and low interaction densities, respectively.[20] Diverse interactions between Eu-NCs promote the formation of long-range ordered structures.

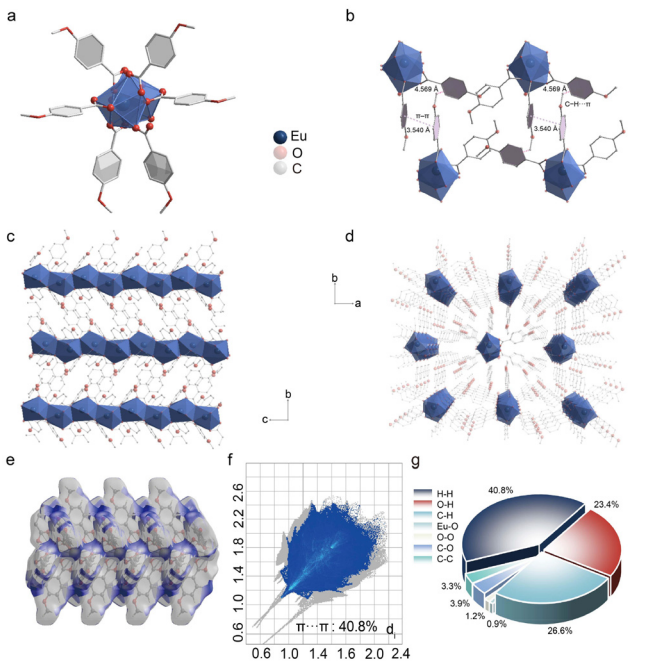

Fig. 1 Crystal structure analysis of the Eu-NC. (a) The smallest symmetric unit and the coordination environment of the Eu^{3+} ion. (b) Cooperative π–π stacking and weak C–H···π contacts in the Eu-NC framework. (c) View of the 3D framework down the *a*-axis. (d) View of the 3D framework down the *c*-axis. (e) The schematic of non-covalent interactions for the Eu-NC. (f) The two-dimensional fingerprint plots, showing the percentage of the non-covalent interaction in the Eu-NC. (g) The ratio of atomic interaction bonds for the Eu-NC.

To further study the crystallization quality and stability, powder X-ray diffraction (PXRD) was first performed (Fig. S3). The PXRD pattern exhibits sharp and intense diffraction peaks, demonstrating the Eu-NC's excellent crystalline quality. All experimental diffraction peaks are in good agreement with the simulation based on the SCXRD data. The agreement validates the phase purity of the bulk isostructural materials. Scanning electron microscopy (SEM) characterization further reveals that the Eu-NCs possess well-defined 1D microrod morphologies with smooth and continuous surfaces (Fig. S4a). Energy-dispersive X-ray spectroscopy (EDX) elemental mapping confirms the homogeneous distribution of constituent elements throughout the microrods (Fig. S4b). Finally, thermal stability measurement shows that the Eu-NC remains intact up to approximately 370 °C as shown by the thermogravimetric analysis (TGA) (Fig. S5).

Beyond high degrees of orderliness, favoring reduction of the photon transmission loss, the waveguide performance also depends on the luminescence properties of Eu^{3+} ions, which are closely related to non-radiative quenching, lattice symmetry and the crystal field environment. At room temperature, the Eu-NC exhibits strong luminescence with peak positions at 585–602 nm ($^5D_0 \rightarrow {}^7F_1$), 609–629 nm ($^5D_0 \rightarrow {}^7F_2$), 649–658 nm ($^5D_0 \rightarrow {}^7F_3$), and 685–708 nm ($^5D_0 \rightarrow {}^7F_4$) under 319 nm excitation (Fig. 2a). The $^5D_0 \rightarrow {}^7F_1$ of Eu^{3+} is known to be magnetic-dipole transition (MDT) allowed and insensitive to the host matrix's structure. In contrast, the $^5D_0 \rightarrow {}^7F_2$ lines are electric dipole transitions (EDT), which are exquisitely responsive to the local site symmetry.[21] The evaluation of the local coordination environment symmetry of the Eu^{3+} ion is quantified by the intensity ratio between its $^5D_0 \rightarrow {}^7F_2$ and $^5D_0 \rightarrow {}^7F_1$ transitions. The value of the asymmetry ratio is 6.18 for the Eu-NC crystal, which is slightly higher than those observed previously, indicating the lower symmetry of the Eu-NC crystals, thus improving the EDT emission intensity.

Through monitoring the excitation spectrum at 616 nm, it was found that a wide excitation band appeared in the range

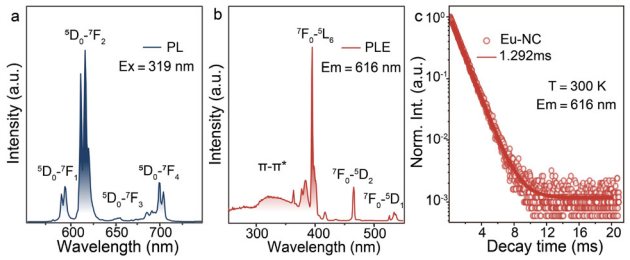

Fig. 2 Photoluminescence of the Eu-NC. (a) Emission spectrum of the Eu-NC under ambient conditions upon excitation at 319 nm. (b) Excitation spectrum of the Eu-NC under ambient conditions upon emission at 616 nm. (c) The decay curve of the Eu-NC was monitored at 616 nm under ambient conditions.

of 270–370 nm, which should correspond to the sensitization region of the ligand (Fig. 2b). Furthermore, using ligand-directed excitation (319 nm) and different intrinsic excitation wavelengths of Eu^{3+} (394 nm, 465 nm, 534 nm), the emission spectrum profiles of the Eu-NC were found to remain consistent, demonstrating the exceptional luminescence stability of the Eu-NC (Fig. S6). In order to prove the sensitization ability of the ligand, we tested the absorption and emission spectra of the ligand (Fig. S7). The main absorption and emission of the ligand are located in the 250–325 nm and 350–500 nm ranges, matching well with the wide excitation band of the Eu-NC. Of note, the total absence of ligand emission signals in the Eu-NC emission spectrum confirms the effective intramolecular sensitization for Eu^{3+} luminescence. Therefore, the MOBA ligands in the system function not only as protective peripheral ligands but also as basic antennas to sensitize luminescence. Fig. S8 shows the sensitization mechanism from the MOBA ligand to Eu^{3+} ions, as dictated by their relative energy level alignment. The room-temperature decay lifetime profile of the $^5D_0 \rightarrow {}^7F_2$ transition was adequately described by a single-exponential function, corresponding to a value of 1.29 ms (Fig. 2c). The Eu-NC shows a photoluminescence quantum yield (PLQY) of ~51.2%, indicating the presence of non-radiative interference.

To unravel the non-radiative transition mechanism of the Eu-NC, we performed PL measurements as a function of temperature in the range of 20–300 K (Fig. 3a and S9). Temperature-dependent studies reveal that both ligand-mediated excitation (~270–370 nm, Peak I) and direct Eu^{3+} intrinsic excitation ($^7F_0 \rightarrow {}^5L_6$ transition, Peak II) exhibit thermal quenching behavior. This phenomenon is principally due to thermally activated phonon-assisted nonradiative decay processes.[22–24] Of note, comparative analysis demonstrates that the luminescence contribution from Peak I displays a more pronounced temperature sensitivity than Peak II (Fig. 3b). As indicated by Fourier transform infrared (FTIR) absorption spectroscopy, the coordinated carboxylate ligands exhibit strong and abundant vibration characteristics, which should play a dominant role in the non-radiative loss of Eu^{3+} excited states (Fig. S10). Specifically, elevated temperatures provide sufficient thermal energy to enhance lattice vibrations, particularly affecting the vibrational

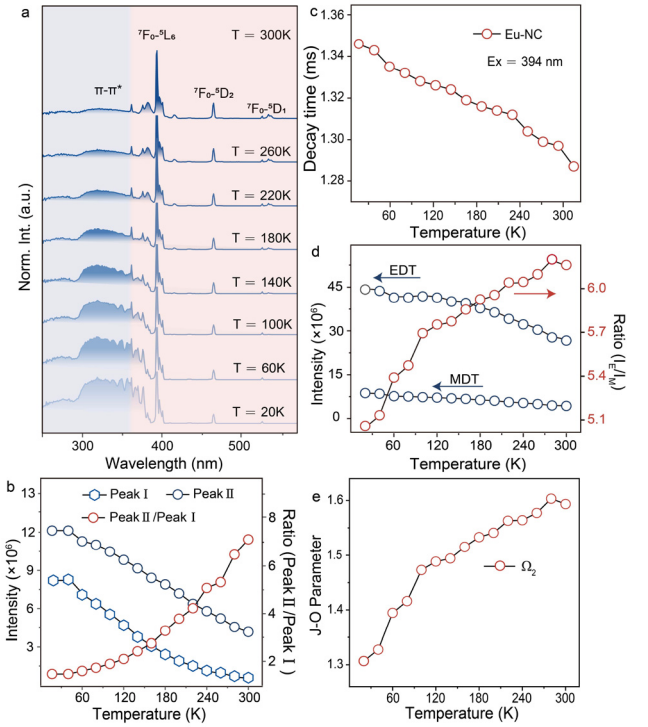

Fig. 3 Investigation of temperature-dependent photophysical mechanisms. (a) Temperature-resolved excitation spectra of Eu-NC under emission at 616 nm (20–300 K). (b) Effect of temperature on different excited states under emission at 616 nm (20–300 K): Peak I – 319 nm, Peak II – 394 nm. (c) The decay time of the Eu-NC monitored at 616 nm (20–300 K). (d) Emission evolution of EDT and MDT (20–300 K). (e) Judd–Ofelt intensity parameters Ω_2 of the Eu-NC (20–300 K).

modes of carboxylate and methoxy functional groups in the MOBA ligand. These high-frequency vibrational modes serve as prominent non-radioactive sources of ligand-to-Eu^{3+} energy transfer. The temperature-dependent decay time measurement provides additional evidence, exhibiting single-exponential behavior across the entire temperature range (20–300 K). The lifetime increases monotonically from 1.29 ms at 300 K to 1.35 ms at 20 K, demonstrating effective suppression of phonon-assisted non-radiative transitions at cryogenic temperatures (Fig. 3c).

Since the photophysical properties of Ln^{3+} ions exhibit a strong dependence on their coordination environment, the increase in emission intensity at low temperatures of the Eu-NC is also related to local site symmetry. To decipher the influence of the local coordination field on the emission spectral characteristics of Eu^{3+} ions, a quantitative Judd–Ofelt analysis was performed to determine the intensity parameters, which are used to reveal effects of short-range covalent interactions.[25,26] At room temperature, the Judd–Ofelt intensity parameters are described by the following established formula, utilizing the ratio of electric dipole to magnetic dipole (ED/MD) transition rates in Ln^{3+}:

$$\frac{A_{ed}}{A_{md}} = \frac{\int I_J(\nu)\mathrm{d}\nu}{\int I_{md}(\nu)\mathrm{d}\nu} = \frac{e^2}{S_{md}}\frac{{\nu_J}^3}{{\nu_{md}}^3}\frac{(n^2+2)^2}{9n^2}$$

$$\Omega_{J'}|\langle \psi J||U^{(J')}||\psi' J'\rangle|^2 \quad (J = 2, 4)$$

where A_{ed} and A_{md} on the left of the equation are the electric dipole transition and magnetic dipole transition rates, respectively, $\int I_J(\nu)\mathrm{d}\nu$ and $\int I_{md}(\nu)\mathrm{d}\nu$ represent the integral emission intensity of the electric dipole transition and the integral intensity of the magnetic dipole transition, respectively. In addition, ν_J and ν_{md} are the central frequencies of the electric dipole and magnetic dipole transitions, respectively, n is the crystal refractive index, and $\langle \psi J||U^{(J')}||\psi' J'\rangle$ is the reduced matrix element. The Ω_2 (1.60×10^{-20} cm^{-1}) parameter represents short-range covalent character. The relatively larger value of Ω_2 indicates lower local symmetry around the Eu^{3+} ion, in accordance with the single-crystal X-ray structural determination. The lower local symmetry is conducive to promoting the EDT's forbidden breaking, thus generating strong EDT in the Eu-NC.

The temperature dependence of the EDT and MDT moments is presented in Fig. 3d. Interestingly, both transition intensities increase at cryogenic temperature. The intensity ratio between the Eu-NC EDT and MDT exhibits a declining trend, decreasing from 6.16 at 300 K to 5.05 at 20 K. Judd–Ofelt analysis further validated the trend, with the Ω_2 parameter decreasing from 1.59 at 300 K to 1.31 at 20 K, unambiguously confirming the progressively elevated local symmetry around Eu^{3+} sites at lower temperatures (Fig. 3e).[27] This indicates that the fundamental cause of enhanced luminescence at low temperatures lies in the suppression of phonons.

To weigh the coordination field effect on luminescence, we further analyzed the crystal field environment of Eu^{3+} ions, residing as J-mixing states. This J-mixing effect enhances the transition intensities of Ln^{3+} ions by relaxing the selection rules based on the J quantum number. The strength of this crystal field perturbation can be quantified by the following equation:

$$\frac{I_{00}}{I_{02}} = \frac{4{B_{20}}^2}{75{\Delta_{20}}^2}$$

where Δ_{20} denotes the energy separation from the $^7F_0$ to $^7F_2$ level, and B_{20} represents the second-order parameter governing the extent of wavefunction mixing. The measured intensity ratio of I_{00} and I_{02} (I_{00}/I_{02}) was 0.0072 and the corresponding crystal field strength B_{20} parameter was found to be 382 cm^{-1} (Fig. S11).[28,29] The significantly smaller magnitude of the B_{20} parameter, compared to those in typical lanthanide complexes, indicates a lower crystal field perturbation. This reduction is generally associated with a lower rate of nonradiative transitions. To this end, the Eu-NC luminescence is a joint consequence of non-radiative relaxation, lattice symmetry, and the crystal field environment.

The well-ordered spatial organization of Eu^{3+} ions within the crystalline matrix prompted us to investigate their anisotropic luminescence properties through polarization-dependent investigation.[30–32] As is well-established in photophysics, the optical characteristics of emitters are fundamentally governed by two critical factors: (i) the molecular geometry packing and (ii) the orientation of transition dipole moments. The polarization measurements, obtained by systematically rotating the polarizer to different polarization angles θ (0–360°), reveal distinct anisotropic emission profiles (Fig. 4a–c and S12). Notably, the luminescence from Eu^{3+} ions exhibits exceptional polarization characteristics, *i.e.*, each narrow sublevel transition ($^5D_0 \rightarrow {}^7F_{1,2}$) maintains its unique polarization configuration despite the splitting of energy level. The polarization difference in Eu^{3+} energy level splitting peaks originates from the relative orientation between the transition matrix elements and the direction of the localized field. For quantitative analysis, the degree of polarization (DOP) was explored, defined by $(I_{max} - I_{min})/(I_{max} + I_{min})$,[33,34] where I_{max} and I_{min} represent the luminescence intensities measured with the polarizer aligned parallel and orthogonal to the orientation axis, respectively. The results indicate that the emission is not completely linearly polarized (DOP < 100%). Detailed analysis shows that individual sharp emission peaks, corresponding to transitions between the crystal-field energy levels of the Eu^{3+} excited and ground states, display varying polarization components (Fig. 4d–h). Peak i and Peak ii correspond to the MDT of $^5D_0 \rightarrow {}^7F_1$, and the degrees of polarization are 18% and 12%, respectively. Peaks iii–v correspond to the EDT of $^5D_0 \rightarrow {}^7F_2$, and the degrees of polarization are 10%, 16% and 18%. This phenomenon directly originates from the anisotropic site of the Eu^{3+} centers within the Eu-NC crystalline framework, as confirmed by single-crystal structural analysis.[35–37] Moreover, this polarization splitting directly reflects the crystal field's perturbation of the localized electron cloud distribution.

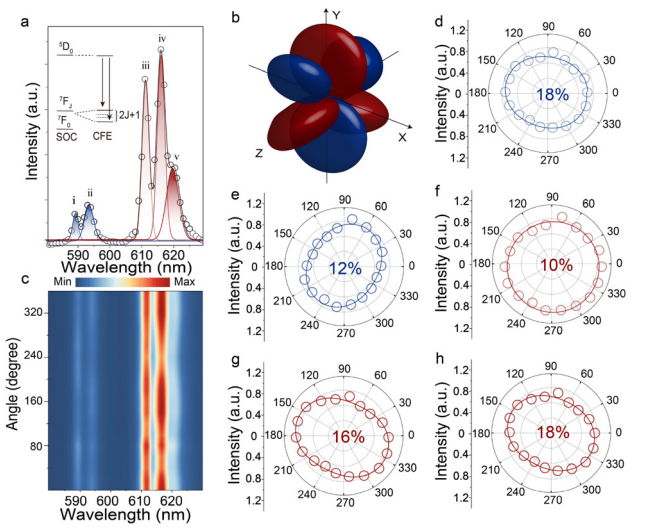

Fig. 4 Polarization properties of the Eu-NC. (a) Spectral fitting of the $^5D_0 \rightarrow {}^7F_1$ (MDT) and $^5D_0 \rightarrow {}^7F_2$ (EDT) transitions was performed using the 0° polarized emission spectrum. The peaks and their corresponding area integrals are assigned distinct colors. Inset: spin–orbit coupling (SOC) and crystal field effect (CFE). (b) Orientation of magnetic transition dipoles and rotors of Eu^{3+} ions in a single crystal of the Eu-NC. (c) Angle-dependent polarized PL spectra of Eu-NC microrods (*ca.* 0–360°). (d–h) Angle-dependent photoemission intensities of the Eu-NC microrods of the selected areas. d–h correspond to the degrees of polarization at peaks i–v in (a): 589, 593, 611, 615, and 620 nm, respectively.

This behavior represents a distinctive advantage of lanthanide-based emitters compared to conventional luminescent materials. Unlike the broadly polarized emission observed in organic fluorophores or quantum dots, where polarization typically reflects the ensemble average of randomly oriented dipoles, each transition in Ln^{3+} ions preserves an intrinsic polarization signature. The transition-specific polarization properties combined with the characteristic sharp-line emissions make lanthanide NCs particularly valuable for applications requiring polarized light sources or orientation-sensitive detection.

The molecular packing arrangement and crystalline organization fundamentally determine the polarized photoluminescence characteristics, becoming a critical factor for developing integrated photonic devices such as optical waveguides and communication components. As mentioned above, these well-defined nanostructures exhibit exceptional morphological uniformity with smooth surfaces and minimal structural defects, as evidenced by high-resolution microscopy studies. These superior structural characteristics would directly contribute to their outstanding waveguide performance.

When excited with UV light, the crystals demonstrate remarkable waveguiding behavior, characterized by intense luminescent spots exclusively at the terminal ends and negligible axial light leakage (Fig. 5a). The absence of side-scattering losses further confirms both the high optical quality and exceptional crystallinity of these materials. This observation indicates: (1) efficient propagation of PL emission along the crystalline axis and (2) excellent optical confinement within the waveguide structure. Consequently, a more detailed characterization study of the waveguide performance was conducted.

Near-field scanning optical microscopy was used to acquire the PL microscopy images and distance-dependent PL spectra of the microrods (Fig. 5b). The laser beam (375 nm) was employed at various locations of the crystal with a gradient of 20 μm, and the spatially resolved PL spectrum was obtained by detecting the excitation position and the endpoint position. The tip emission intensity of the microrod exhibited a monotonic decay with propagation distance; however, spectral profiles exhibited no change across the different excitation points. To quantify the crystal optical loss, we calculated the optical loss coefficient (R) using a single exponential fitting method: $I_{tip}/I_{body} = A\exp(-R/D)$, where I_{tip}/I_{body} denotes the ratio of the photoluminescence intensities collected at the emitting tip and the excited body site, respectively. D is defined as the separation distance from the excitation site to the emitting tip (Fig. 5c). Notably, the measured loss coefficients of the waveguides demonstrated a pronounced positional dependence, attributed to spatial variations in transition dipole moments at different emission sites. Specifically, the magnetic dipole peak corresponds to loss coefficients of 1.1×10^{-2} dB μm^{-1} and 3.1×10^{-3} dB μm^{-1}. The electric dipole peak corresponds to loss coefficients of 7.3×10^{-3} dB μm^{-1}, 1.4×10^{-2} dB μm^{-1}, and 6.4×10^{-3} dB μm^{-1}. The lowest coefficient 6.4×10^{-3} dB μm^{-1} surpasses reported values for inorganic, organic, and hybrid rare earth materials.[38–40] The low optical loss observed in these Eu-NC microrods arises from their high crystallinity, smooth surfaces, and consistent alignment between transition dipole moments and crystal orientation.

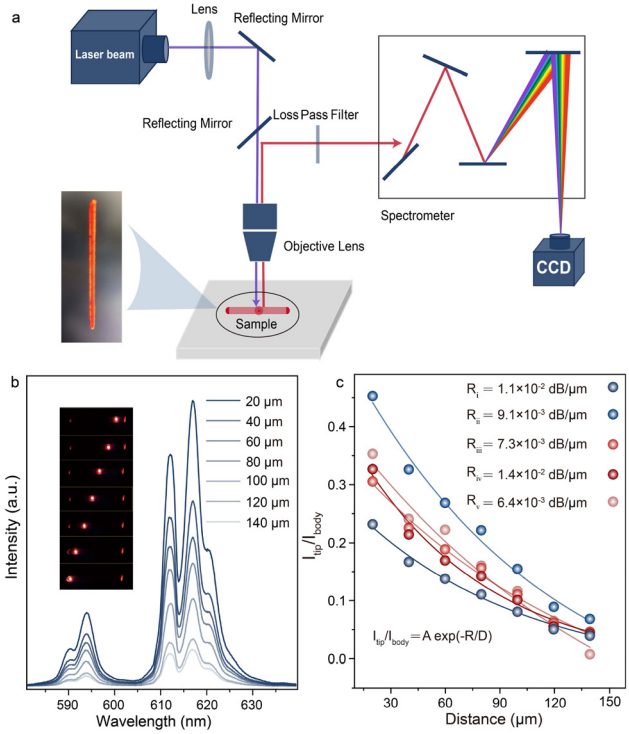

Fig. 5 Optical waveguide of the Eu-NC. (a) Schematic of the optical waveguide experimental setup to obtain photoluminescence microscope images of the Eu-NC. (b) Spatially resolved PL spectra from the Eu-NC microrod tip as a function of excitation distance. Insert: The PL image obtained from Eu-NC crystal. (c) The optical-loss coefficients (R) for different peaks correspond to the splitting peak positions of $^5D_0 \rightarrow {}^7F_1$ and $^5D_0 \rightarrow {}^7F_2$, respectively.

Conclusions

We synthesized a Eu-NC *via* hydrothermal synthesis and showed good optical waveguide functionality through crystallographic alignment and luminescence behavior. Significantly, directional photon transport with a low waveguide loss coefficient of 6.4×10^{-3} dB μm^{-1} was obtained. These findings highlight the potential of crystallized lanthanide NCs as engineered platforms for integrated photonics, particularly in wavelength-selective optical circuits and reconfigurable micro-opto-electronic systems.

Author contributions

J. Xia: writing – original draft, data curation. W. Dong: writing – original draft and data curation. S. He: investigation. F. Jiang: data curation. W. Tian: data curation. Q. Sun: data curation. M. Hong: investigation. L. Meng: investigation,

Y. Zhang: investigation. Z. Wu: supervision, resources, funding acquisition, and conceptualization. X. Bai: supervision, resources, funding acquisition, and conceptualization.

Conflicts of interest

There are no conflicts to declare.

Data availability

The data that support the findings of this study are available from the corresponding author upon reasonable request.

Supplementary information (SI) is available. See DOI: https://doi.org/10.1039/d5qi02356d.

CCDC 1459317 contains the supplementary crystallographic data for this paper.[41]

Acknowledgements

The authors sincerely acknowledge the financial support from the National Key R&D Program of China (2024YFE0206100) and the National Natural Science Foundation of China (T2325015, U21A2068, and T2521005 to X. B., and 12174151 and 12574440 to Z. W).

References

1 P. Xu, B. Cui, Y. Bu, H. Wang, X. Guo, P. Wang, Y. Sheng and L. Tong, Elastic ice microfibers, *Science*, 2021, **373**, 187–192, DOI: 10.1126/science.abh3754.

2 N. Karimi, M. Virkki, A. Alberucci, O. Buchnev, M. Kauranen, A. Priimagi and G. Assanto, Molding Optical Waveguides with Nematicons, *Adv. Opt. Mater.*, 2017, **5**, 1700199, DOI: 10.1002/adom.201700199.

3 J. Kim, J. Song, H. Ryu and C. Ah, Electrochromic Infrared Light Modulation in Optical Waveguides, *Adv. Opt. Mater.*, 2019, **8**, 1901464, DOI: 10.1002/adom.201901464.

4 D. Wang, M. Kuzma, X. Tan, T. He, C. Dong, Z. Liu and J. Yang, Phototherapy and optical waveguides for the treatment of infection, *Adv. Drug Delivery Rev.*, 2021, **179**, 114036, DOI: 10.1016/j.addr.2021.114036.

5 J. Xiao, T. Zhou, N. Yao, S. Ma, C. Pan, P. Wang, H. Fu, H. Liu, J. Pan, L. Yu, S. Wang, W. Yang, L. Tong and L. Zhang, Optical fibre taper-enabled waveguide photoactuator, *Nat. Commun.*, 2022, **13**, 363, DOI: 10.1038/s41467-022-28021-4.

6 S. Yalamanchili, E. Verlage, W. Cheng, K. Fountaine, P. Jahelka, P. Kempler, R. Saive, N. Lewis and H. Atwater, High Broadband Light Transmission for Solar Fuels Production Using Dielectric Optical Waveguides in TiO_2 Nanocone Arrays, *Nano Lett.*, 2019, **20**, 502–508, DOI: 10.1021/acs.nanolett.9b04225.

7 P. Zhao, V. Shekhawat, M. Girardi, Z. He, V. Torres-Company and P. Andrekson, Ultra-broadband optical amplification using nonlinear integrated waveguides, *Nature*, 2025, **640**, 918–923, DOI: 10.1038/s41586-025-08824-3.

8 X. Ye, Y. Liu, Q. Guo, Q. Han, C. Ge, S. Cui, L. Zhang and X. Tao, 1D versus 2D cocrystals growth via microspacing in-air sublimation, *Nat. Commun.*, 2019, **10**, 761, DOI: 10.1038/s41467-019-08712-1.

9 D. Sirbuly, M. Law, H. Yan and P. Yang, Semiconductor Nanowires for Subwavelength Photonics Integration, *J. Phys. Chem. B*, 2005, **109**, 15190–15213, DOI: 10.1021/jp051813i.

10 C. Zhang, Y. Yan, Y. Zhao and J. Yao, From Molecular Design and Materials Construction to Organic Nanophotonic Devices, *Acc. Chem. Res.*, 2014, **47**, 3448–3458, DOI: 10.1021/ar500192v.

11 C. Sun, Z. Gao, K. Teng, L. Niu, Y. Chen, Y. Zhao and Q. Yang, Supramolecular Polymer-Based Fluorescent Microfibers for Switchable Optical Waveguides, *ACS Appl. Mater. Interfaces*, 2018, **10**, 26526–26532, DOI: 10.1021/acsami.8b08490.

12 D. Bose, M. Harrington, A. Isichenko, K. Liu, J. Wang, N. Chauhan, Z. Newman and D. Blumenthal, Anneal-free ultra-low loss silicon nitride integrated photonic, *Light: Sci. Appl.*, 2024, **13**, 156, DOI: 10.1038/s41377-024-01503-4.

13 J. Zhang, Y. Kang, X. Guo, Y. Li, K. Liu, Y. Xie, H. Wu, D. Cai, J. Gong, Z. Shi, Y. Jin, P. Wang, E. Fang, L. Zhang and L. Tong, High-power continuous-wave optical waveguiding in a silica micro/nanofibre, *Light: Sci. Appl.*, 2023, **12**, 89, DOI: 10.1038/s41377-023-01109-2.

14 C. Xu, Y. Yu, Q. Lv, C. Yan, X. Wang and L. Liao, Rational self-assembly of polygonal organic microcrystals for shape-dependent multi-directional 2D optical waveguides, *Chin. Chem. Lett.*, 2022, **33**, 3255–3258, DOI: 10.1016/j.cclet.2021.10.076.

15 Q. Chen, B. Tang, K. Ye, H. Hu and H. Zhang, Ultra-Wide Modulation and Reversible Reconfiguration of a Flexible Organic Crystalline Optical Waveguide Between 645 and 731 nm, *Angew. Chem., Int. Ed.*, 2024, **64**, e202417459, DOI: 10.1002/anie.202417459.

16 M. Qian, Y. Sun, Z. Hu, X. Fang, J. Zhu, X. Fan, Q. Liao, C. Wu and H. Sun, Fluorescent chemo-sensors based on "dually smart" optical micro/nano-waveguides lithographically fabricated with AIE composite resins, *Mater. Horiz.*, 2020, **7**, 1782–1789, DOI: 10.1039/d0mh00249f.

17 J. Li, Y. Guan, W. Xia, J. Chen, J. Huang, Y. Chen, Q. Lin, E. Chen and H. Xie, Highly efficient room temperature phosphorescent liquid crystalline polymer optical waveguides for advanced optoelectronic, *Sci. China: Chem.*, 2024, **67**, 3450–3457, DOI: 10.1007/s11426-024-2126-0.

18 Y. Yan, M. Zhao, F. Jiang, H. Zhu, W. Dong, S. He, J. Xia, M. Hong, Z. Wu and X. Bai, Ligand rigidity-mediated coordination symmetry engineering in lanthanide-titanium nanoclusters achieves >90% photoluminescence quantum yield, *Rare Earths*, 2025, **43**, 1590–1600, DOI: 10.1016/j.jre.2025.06.001.

19 Y. Du and J. Zheng, Syntheses, structures and magnetic properties of a series of lanthanide complexes based on p-methoxybenzoic acid, *Inorg. Chem. Commun.*, 2016, **66**, 59–63, DOI: **10.1016/j.inoche.2016.01.020**.

20 S. Wang, K. Liang, H. Zhao, M. Wu, J. He, P. Wei, Z. Ding, J. Li, X. Huang and Y. Ren, Electronic structure formed by Y_2O_3-doping in lithium position assists improvement of charging-voltage for high-nickel cathodes, *Nat. Commun.*, 2025, **16**, 1, DOI: **10.1038/s41467-024-52768-7**.

21 D. Tu, Y. Liu, H. Zhu, R. Li, L. Liu and X. Chen, Breakdown of Crystallographic Site Symmetry in Lanthanide-Doped $NaYF_4$ Crystals, *Angew. Chem., Int. Ed.*, 2012, **52**, 1128–1133, DOI: **10.1002/anie.201208218**.

22 Y. Kim, J. Mendes, J. Miichelsen, H. Shin, N. Lee, Y. Choi and S. Cushing, Coherent charge hopping suppresses photoexcited small polarons in $ErFeO_3$ by antiadiabatic formation mechanism, *Sci. Adv.*, 2024, **10**, eadk4282, **https://www.science.org/doi/10.1126/sciadv.adk4282**.

23 F. Wang, W. Chu, L. Huber, T. Tu, Y. Dai, J. Wanga, H. Peng, J. Zhao and X. Zhua, Phonon signatures for polaron formation in an anharmonic semiconductor, *Proc. Natl. Acad. Sci. U. S. A.*, 2022, **119**, 30, DOI: **10.1073/pnas.2122436119**.

24 W. Dong, F. Zhang, T. Li, Y. Zhong, L. Hong, Y. Shi, F. Jiang, H. Zhu, M. Lu, Q. Yao, W. Xu, Z. Wu, X. Bai and Y. Zhang, Triple-Phosphorescent Gold Nanoclusters Enabled by Isomerization of Terminal Thiouracils in the Surface Motifs, *J. Am. Chem. Soc.*, 2024, **146**, 22180–22192, DOI: **10.1021/jacs.4c01291**.

25 Y. Zhang, X. Wang, K. Xu, F. Zhai, J. Shu, Y. Tao, J. Wang, L. Jiang, L. Yang, Y. Wang, W. Liu, J. Su, Z. Chai and S. Wang, Near-Unity Energy Transfer from Uranyl to Europium in a Heterobimetallic Organic Framework with Record-Breaking Quantum Yield, *J. Am. Chem. Soc.*, 2023, **145**, 13161–13168, DOI: **10.1021/jacs.3c01968**.

26 X. Li, X. Shen, M. Lu, J. Wu, Y. Zhong, Z. Wu, W. Yu, Y. Gao, J. Hu, J. Zhu, Y. Zhang and X. Bai, Wide-coverage and Efficient NIR Emission from Single-component Nanophosphors through Shaping Multiple Metal-halide Packages, *Angew. Chem., Int. Ed.*, 2023, **62**, e202217832, DOI: **10.1002/ange.202217832**.

27 X. Wang, S. He, F. Lv, X. Wang, M. Hong, L. Cao, G. Zhuang, C. Chen, J. Zheng, L. Long and X. Zheng, Ln^{3+} Induced Thermally Activated Delayed Fluorescence of Chiral Heterometallic Clusters Ln_2Ag_{28}, *Angew. Chem., Int. Ed.*, 2024, **63**, e202410414, DOI: **10.1002/anie.202410414**.

28 Y. Xu, L. Zhao, Y. Guo and Y. Fu, Anomalous intense emission of the $^5D_0/^7F_4$ transition for reddish-orange light-emitting and fluorescent probe for multiple lattice sites in β-PbF_2:Eu^{3+}/K^+ oxyfluoride glass ceramics, *New J. Chem.*, 2024, **48**, 11874–11885, DOI: **10.1039/d4nj01481b**.

29 H. Dong, L. Sun and C. Yan, Local Structure Engineering in Lanthanide-Doped Nanocrystals for Tunable Upconversion Emissions, *J. Am. Chem. Soc.*, 2021, **143**, 20546–20561, DOI: **10.1021/jacs.1c10425**.

30 P. Li, Y. Guo, A. Liu, X. Yue, T. Yuan, J. Zhu, Y. Zhang and F. Li, Deterministic Relation between Optical Polarization and Lattice Symmetry Revealed in Ion-Doped Single Microcrystals, *ACS Nano*, 2022, **16**, 9535–9545, DOI: **10.1021/acsnano.2c02756**.

31 J. Kim, R. Chacón, Z. Wang, E. Larquet, K. Lahlil, A. Leray, G. Colas-des-Francs, J. Kim and T. Gacoin, Measuring 3D orientation of nanocrystals via polarized luminescence of rare-earth dopants, *Nat. Commun.*, 2021, **12**, 1943, DOI: **10.1038/s41467-021-22158-4**.

32 C. Brecher, H. Samelson, A. Lempicki, R. Riley and T. Peters, Polarized Spectra and Crystal-Field Parameters of Eu^{3+} in YVO_4, *Phys. Rev.*, 1967, **155**, 178–187, DOI: **10.1103/physrev.155.178**.

33 D. Yan, H. Yang, Q. Meng, H. Lin and M. Wei, Two-Component Molecular Materials of 2,5-Diphenyloxazole Exhibiting Tunable Ultraviolet/Blue Polarized Emission, Pump-enhanced Luminescence, and Mechanochromic Response, *Adv. Funct. Mater.*, 2013, **24**, 587–594, DOI: **10.1002/adfm.201302072**.

34 G. Fan and D. Yan, Two-Component Orderly Molecular Hybrids of Diphenylanthracene: Modulation of Solid-State Aggregation toward Tunable Photophysical Properties and Highly Enhanced Electrochemiluminescenc, *Adv. Opt. Mater.*, 2016, **4**, 2139–2147, DOI: **10.1002/adom.201600310**.

35 X. Wang, B. Yin, L. Jiang, C. Yang, Y. Liu, G. Zou, S. Chen and M. Zhu, Ligand-protected metal nanoclusters as low-loss, highly polarized emitters for optical waveguides, *Science*, 2023, **381**, 784–790, DOI: **10.1126/science.adh2365**.

36 X. Yang, X. Lin, Y. Zhao, Y. Zhao and D. Yan, Lanthanide Metal–Organic Framework Microrods: Colored Optical Waveguides and Chiral Polarized Emission, *Angew. Chem., Int. Ed.*, 2017, **56**, 7853–7857, DOI: **10.1002/anie.201703917**.

37 C. Zhou, W. Huang, K. Kuang, Z. Li, S. Chen, Y. Kuai and M. Zhu, Low Optical Loss and Bent Waveguides: Crystals of a One-Dimensional Pt_1Ag_{14} Nanocluster, *ACS Nano*, 2025, **19**, 13230–13239, DOI: **10.1021/acsnano.5c00359**.

38 L. Fei, Z. Lv, S. Chen, Y. Tao, L. Qiu, C. Han, X. Wang and H. Xu, Ordered and Anisotropic Assembling of Au_2Ag_2 Parallelogram Enables Multi-Directional Low-Loss Optical Waveguide, *Adv. Funct. Mater.*, 2025, e30393, DOI: **10.1002/adfm.202530393**.

39 S. Min, A. Dhamsaniya, L. Zhang, G. Hou, Z. Huang, K. Pambhar, A. Shah, V. Mehta, Z. Liu and B. Song, Scale Effect of a Fluorescent Waveguide in Organic Micromaterials: A Case Study Based on Coumarin Microfibers, *J. Phys. Chem. Lett.*, 2019, **10**, 5997–6002, DOI: **10.1021/acs.jpclett.9b02315**.

40 M. Song, Y. Dang, J. Dong, X. Zhang, S. Lei and W. Hu, Eu-based coordination polymer microrods for low-loss optical waveguiding application, *Nanoscale*, 2019, **11**, 21061, DOI: **10.1039/c9nr07494e**.

41 CCDC 1459317: Experimental Crystal Structure Determination, 2025, DOI: **10.5517/ccdc.csd.cc1kzjrt**.